JAAS

PAPER

View Article Online
View Journal | View Issue

Cite this: *J. Anal. At. Spectrom.*, 2017, **32**, 2341

Accurate determination of sulfur isotopes ($\delta^{33}S$ and $\delta^{34}S$) in sulfides and elemental sulfur by femtosecond laser ablation MC-ICP-MS with non-matrix matched calibration†

Jiali Fu,[a] Zhaochu Hu,*[a] Jianwei Li,[a] Lu Yang,[b] Wen Zhang,[a] Yongsheng Liu,[a] Qiuli Li,[c] Keqing Zong[a] and Shenghong Hu[a]

The isotopic composition of sulfur is a vital tracer used in the Earth and planetary sciences. In this study, the laser- and ICP-induced isotopic fractionation in S-rich minerals (sulfides and elemental S) with different matrices was investigated by using 257 nm femtosecond (fs) and 193 nm ArF excimer nanosecond (ns) laser ablation systems coupled to a Neptune Plus MC-ICP-MS. Compared to ns-LA-MC-ICP-MS, higher sensitivity (1.4–2.4 times) under similar instrumental conditions and better precision (~1.6-fold) under the same signal intensity condition were achieved by fs-LA-MC-ICP-MS. In addition, a fs-laser provides less fluence and matrix dependent S isotopic fractionation, and more stable transient isotopic ratios compared to a ns-laser. Better results acquired by fs-LA-MC-ICP-MS were attributed to the smaller size of particles and less thermal effect produced by using the fs-laser, which were evidenced by the morphologies of the ablation craters and ejected aerosol particles of P-S-1 (the pressed powder pellet of IAEA-S-1) and PPP-1 (a pyrite single crystal from the Sukhoi Log deposit). The ICP-induced isotopic fractionation (matrix effect) was still found in fs-LA-MC-ICP-MS under the maximum sensitivity conditions. However, a significant reduction of the matrix effect was obtained under robust plasma conditions at a lower makeup gas flow rate (0.52–0.54 l min^{-1}) relative to the maximum sensitivity condition (0.6 l min^{-1}) for S isotope analysis. This could be ascribed to the particles that not only pass into the higher temperature ICP for a longer residence time at a lower makeup gas flow rate that resulted in more efficient vaporization of the particles, but also experience a more robust plasma induced by adding 4–6 ml min^{-1} N_2 into the plasma. Furthermore, under the robust conditions, the results of six reference materials with different matrices obtained by fs-LA-MC-ICP-MS with non-matrix matched calibration with a spot size of 20–44 μm showed excellent agreement with the reference values (the accuracy of 0.01–0.15‰ for $\delta^{34}S$ and 0.11–0.45‰ for $\delta^{33}S$ and the precision of 0.16–0.40‰ (2 s) for $\delta^{34}S$ and 0.35–0.78‰ (2 s) for $\delta^{33}S$) and the mass-dependent fractionation line, validating the applicability of the proposed approach for providing high-quality *in situ* isotope data ($\delta^{33}S$ and $\delta^{34}S$) of sulfides and elemental sulfur at high spatial resolution using non-matrix matched analysis.

Received 16th August 2017
Accepted 26th September 2017

DOI: 10.1039/c7ja00282c

rsc.li/jaas

1. Introduction

Laser ablation multi-collector inductively coupled plasma mass spectrometry (LA-MC-ICP-MS) allows for *in situ* analysis of isotopic composition at high spatial resolution, offering a powerful tool for measuring geological samples with small sizes or complex textures such as mineral growth zonation, recrystallization and metasomatism preserved at the micro-scale.[1–4] Sulfur isotopes are of particular interest because sulfur isotopes can serve as a vital tracer in the Earth and planetary sciences.[5] Sulfur is a widely distributed element on the Earth and in the solar system. Its multiple valence states of −2 to +6 allow it to participate in numerous geochemical and biochemical processes.[6] Naturally occurring sulfur has four stable isotopes, ^{32}S, ^{33}S, ^{34}S and ^{36}S, with abundances of 94.99, 0.75, 4.25 and 0.01%, respectively.[7] Studies have shown that considerable sulfur isotope fractionation occurs in the natural environment and the overall isotopic variability of $\delta^{34}S$ generally ranges from at least −50 to +40.[8] A sensitive analytical

[a]State Key Laboratory of Geological Processes and Mineral Resources, Faculty of Earth Resources, China University of Geosciences, Wuhan 430074, China. E-mail: zchu@vip.sina.com; Fax: +86 27 67885096; Tel: +86 27 61055600

[b]National Research Council Canada, 1200, Montreal Rd., Ottawa, Ontario, K1A 0R6, Canada

[c]State Key Laboratory of Lithospheric Evolution, Institute of Geology and Geophysics, Chinese Academy of Sciences, Beijing 100029, China

† Electronic supplementary information (ESI) available. See DOI: 10.1039/c7ja00282c

technique is vital to advance applications of S stable isotopes (^{32}S, ^{33}S, and ^{34}S) as a sensitive tracer in diverse fields of geosciences.[9,10] However, bulk analysis methods (*e.g.*, GS-MS and MC-ICP-MS)[11,12] would be unsatisfactory in applications for sulfur isotope analyses in tiny individual minerals or zones within minerals to provide key constraints on the sulfur cycle in relevant studies.[9,10,13] Thus, an *in situ* analytical approach for isotope determination is preferred for many applications.

In general, *in situ* analytical techniques for S isotopes include LA-MC-ICP-MS (<0.45‰, 2 s)[14,15] and secondary ion mass spectrometry (SIMS) (<0.2‰, 2 s),[16] allowing high precision isotopic analysis with a high spatial resolution of 10–60 μm. Although SIMS analysis provides higher spatial resolution than LA-MC-ICP-MS, this technique is not widely available and its instrumental mass fractionation is intrinsically linked to the composition and crystallographic orientation of the material being analyzed which leads to serious matrix effects.[16,17] LA-MC-ICP-MS allows for *in situ* and rapid analysis at high spatial resolution with a lower detection limit and has been recognized as an efficient, less sample matrix dependent and relatively widespread tool for *in situ* analysis of isotopes.[4,18] However, serious matrix effects on S isotopic analysis occurred in ns-LA-(MC)-ICP-MS between different matrices,[14,19,20] which are particularly significant at high spatial resolution analysis. Therefore, a matrix-matched standard is usually necessary for the accurate determination of S isotope ratios by ns-LA-(MC)-ICP-MS. Bendall *et al.* (2006)[21] used an in-house standard of pyrite as a matrix-matched external standard to calibrate the instrumental mass fractionation, achieving an external precision of 0.32‰ (2 s) for δ^{34}S measured by ns-LA-MC-ICP-MS. Craddock *et al.* (2008)[20] proposed an approach to correct the instrumental mass fractionation by introducing a matrix-matched solution standard during laser ablation sampling in ns-LA-MC-ICP-MS, and achieved an external precision of 0.45‰ (2 s) for δ^{34}S of anhydrite standard Sch-M-2. However, this method is more complicated and requires a time-consuming sample preparation process. Gilbert *et al.* (2014)[22] developed an in-house pyrite reference material (PPP-1) for S isotope analysis. Their results showed that significant matrix effects between pyrite and bornite can be reduced with increasing fluence using ns-LA-ICP-MS to a certain extent, and a precision of ~1‰ (RSE) for δ^{34}S was obtained. Fu *et al.* (2016)[15] adopted a line scan ablation mode at appropriate fluence for the reduction of sulfur isotopic fractionation during the ablation process and matrix effect among certain S-rich samples (IAEA-S-1, pyrite, chalcopyrite, sphalerite, elemental S, molybdenite, and MASS-1). A precision of 0.15–0.45‰ (2 s) for δ^{34}S was obtained by ns-LA-MC-ICP-MS. For high spatial resolution analysis in single spot ablation mode, a matrix-matched reference material was highly recommended. Zhu *et al.* (2016)[23] reported up to 2‰ fractionation for δ^{34}S with different laser parameters during analysis of pyrite using a 193 nm ArF excimer ns-laser, and the ablated particles of pyrite decomposed into two phases with different δ^{34}S values during the ablation process. Their results reinforce the importance of matrix-matched calibration for sulfur isotope analysis using ns-LA-MC-ICP-MS.

Many previous studies have shown that a fs-laser might be less prone to laser-induced elemental/isotopic fractionation and matrix-related problems in comparison with a ns-laser.[24–26] This is because the pulse width of the fs-laser is shorter than the electron-phonon relaxation time, eliminating heating effects and avoiding laser plasma interaction during the ablation process. In contrast, ns-laser ablation tends to cause significant heating and melting, because the pulse width of the ns-laser is too long to prevent electron-lattice heat transfer.[27,28] For example, Možná *et al.* (2006)[26] compared the performance of UV-fs-LA-ICP-MS and UV-ns-LA-ICP-MS for iron-based samples; higher sensitivity (25–30%), more stable elemental ratios (10%, TRSD) and more accurate results (5–15%) with non-matrix matched calibration for elemental analysis were obtained by UV-fs-LA-ICP-MS. Horn and Blanckenburg (2007)[24] reported that laser-induced isotopic fractionation was undetectable for Fe isotopes and the accuracy of the results was independent of the matrix when using fs-LA-MC-ICP-MS, while an isotopic ratio drift up to several ‰ was evident during the ns-laser ablation process. Horn *et al.* (2006)[3] and Chmeleff *et al.* (2008)[29] successfully analyzed Fe and Si isotopes in sulfides, oxides and silicates using non-matrix-matched calibration (IRMM-014 and IRMM-017 as the external calibrators for Fe and Si, respectively) by UV-fs-LA-MC-ICP-MS. To date, only Chen *et al.* (2016)[30] have applied the fs-laser coupled to Nu Plasma MC-ICP-MS for *in situ* analysis of S isotopes, and found that matrix effects were significant when using IAEA-S-1 (even using chalcopyrite glass as a calibrator) as a standard to calibrate natural chalcopyrite with the spot size of 20 μm and the laser fluence of 0.4 J cm^{-2}. Therefore, the nature of matrix-related effects is still enigmatic for *in situ* analysis of S isotopes using fs-LA-MC-ICP-MS at high spatial resolution.

It is well known that isotopic fractionation not only originates during laser ablation, but also occurs within the ICP during vaporization, atomization and ionization.[31–33] Jackson and Günther (2003)[31] reported a large bias for the isotopic composition of the target sample for Cu isotope ratios by on-line ns-LA-MC-ICP-MS at high laser fluence, but this isotopic fractionation can be significantly reduced by filtering larger particles (>0.5 μm) from the ablation aerosol. These observations suggested that isotopic fractionation was predominantly induced by the differential volatilization and ionization of Cu isotopes during insufficient vaporization of large particles in the ICP. Kimura *et al.* (2016)[33] reported that increased ICP sample loading through increasing laser repetition rates and ablation diameters led to an increased fractionation of −8‰ for both δ^{7}Li and δ^{11}B using the 266 nm fs-laser and 193 nm excimer ns-laser, and suggested that the origin of isotope fractionation was primarily induced by the insufficient aerosol vaporization in the ICP that resulted from the mass load effect, as well as from the thermal effect at the laser site for Li and B isotopes. Further studies are necessary to investigate the origin of sulfur isotopic fractionation during the *in situ* analysis process by LA-MC-ICP-MS, especially at high spatial resolution.

In this study, we systematically investigated the effects of laser fluence, spot size and ablation mode on S isotopic fractionation between the fs-laser and ns-laser, and the effects of

the makeup gas flow rate on the matrix effect for sulfur isotope analysis by fs-LA-MC-ICP-MS. In addition, the signal intensity, the stability of transient isotopic ratios and the precision of sulfur isotopes ratios between the fs-laser and ns-laser were compared in detail, along with the morphologies of the ablation craters and the deposited particles produced by using the fs-laser and ns-laser. The final optimized method was validated by analyzing six reference materials of different matrices with non-matrix-matched calibration using fs-LA-MC-ICP-MS.

2. Experimental

2.1 Instrumentation

All isotopic measurements were conducted on a Neptune Plus multiple collector inductively coupled plasma mass spectrometer (MC-ICP-MS, Thermo Fisher Scientific, Germany) in combination with a 257 nm Yb femtosecond (fs) laser ablation system (NWR-Femto^{UC}, USA) and a 193 nm ArF excimer nanosecond (ns) laser ablation system (GeoLas 2005, Lambda Physik, Göttingen, Germany) in the State Key Laboratory of Geological Processes and Mineral Resources, China University of Geosciences in Wuhan. The ns-laser is equipped with an optical configuration producing a constant lateral energy distribution leading to pan-shaped ablation pits on the sample, while there is a Gaussian energy beam profile across its ablation diameter in the fs-laser.[25] The Neptune Plus is a double-focusing MC-ICP-MS with a movable multi-collector array of Faraday cups which permitted the simultaneous detection of ^{32}S, ^{33}S and ^{34}S signals collected in the L3, center and H3 Faraday cups, respectively. Approximately 0.5 l min^{-1} helium was flushed into the ablation cell, which was then mixed with argon (makeup gas) and nitrogen (4–6 ml min^{-1}) *via* a T connector downstream prior to the plasma torch. The amount of additional nitrogen was controlled by using a mass flow controller (Aalborg DFC 26 mass flow controller). To achieve a smooth signal during isotopic ratio determination, a "wave" signal stabilizer device was used in this study.[34] Based on previous study, the use of the Jet sample cone in combination with the X skimmer cone improved the S sensitivity by a factor of 3.6 compared to the standard sample cone combined with the H skimmer cone in ns-LA-MC-ICP-MS. Furthermore, the addition of 4 ml min^{-1} N_2 to the central gas flow was found to significantly suppress the oxide and hydride polyatomic interference on sulfur isotopes and improve the mass bias stability of sulfur isotope ratios at the optimum makeup gas flow rate.[15] The instrumental and data acquisition parameters of the lasers and the MC-ICP-MS are listed in Table 1. The morphologies of the ablation craters and the aerosols deposited around the ablation holes were imaged by scanning electron microscopy (SEM, Quanta 450 FEG, FEI, USA).

Table 1 Typical operating parameters for NEPTUNE MC-ICPMS and laser systems

Mass spectrometer setup		
MC-ICP-MS	NEPTUNE Plus	
RF power	1200 W	
Pt-guard electrode	On, grounded	
Plasma Ar gas flow rate	16.0 l min^{-1}	
Auxiliary Ar gas flow rate	0.85 l min^{-1}	
Ar makeup gas flow rate	0.46–0.64 l min^{-1}	
N_2 gas flow rate	4–6 ml min^{-1}	
Interface cones	Jet sample cone + X skimmer cones (Ni)	
Data acquisition parameters		
Acquisition type	Static	
Detection system	Nine Faraday cups	
Cup configuration	^{32}S (L3), ^{33}S (C), ^{34}S (H3)	
Resolution mode	Medium resolution (~4000)	
Signal integration time	0.262 s	
Signal analysis protocol	1 Block 200 cycles	
Laser setup		
Laser	ArF 193 nm laser	Yb:YAG femtosecond laser
Pulse length	15 ns	300 fs
Carrier gas	Helium (0.5 l min^{-1})	Helium (0.5 l min^{-1})
Ablation mode	Single spot and line scan	Single spot and line scan
Ablation diameter	24–44 μm	20–44 μm
Ablation duration	34 s	34 s
Pulse rate	3 Hz	3 Hz
Fluence	1.8–4.2 J cm^{-2}	0.85–2.82 J cm^{-2}

2.2 Preparation of samples

The well-characterized reference materials are listed in Table 2. All the pulverized reference materials including IAEA-S-1, IAEA-S-2, IAEA-S-4, GBW07268, and GBW07270 were analyzed as cold pressed powder pellets prepared by using a presser without the addition of a binder applying 300 kN (~1 × 10^6 kPa) for 5 min. For GBW07268 and GBW07270, the original particles were further ground using agate milling with the particle size of 90% of each sample less than 10 μm.[15] All the samples were fixed with epoxy resin in a plastic tube independently, and then polished with 2 μm diamond paste to give a flat surface prior to LA-MC-ICP-MS analyses.

2.3 Isotope ratio measurements and data reduction

The sulfur isotopes were measured on the shoulder of the interference-free plateau of peaks of ^{32}S, ^{33}S, and ^{34}S (see ESI Fig. S1†), which were obtained at medium mass resolution of MC-ICP-MS (R_{power} (5, 95%) = 4707 as defined in a previous study).[39] Each measurement was performed in static mode consisting of one block of 200 cycles with an integration time of 0.262 s per cycle. All data were collected for 18 s before firing the laser to acquire an average background signal that was subsequently subtracted from the ablation signals collected for the next 34 s during offline data processing. The standard-sample bracketing approach was applied to correct instrumental mass bias by repeatedly measuring the standard before and after every five samples. The final sulfur isotope ratios

Table 2 A list of seven samples studied

Sample name	Material	Description	Reference
IAEA-S-1	Synthetic Ag_2S	Powder, distributed by the International Atomic Energy Agency, Vienna, Austria	35
IAEA-S-2	Synthetic Ag_2S	Powder, distributed by the International Atomic Energy Agency, Vienna, Austria	35
IAEA-S-4	Elemental S	Powder, distributed by the International Atomic Energy Agency, Vienna, Austria	36
GBW07268	Chalcopyrite	Powder, produced by the Institute of Rock and Mineral Analysis, Ministry of Geology and Mineral Resources, China	37
GBW07270	Sphalerite	Powder, produced by the Institute of Rockand Mineral Analysis, Ministry of Geology and Mineral Resources, China	37
PPP-1	Pyrite	Single crystal, from the Sukhoi Log deposit, Russia	22
MASS-1	Synthetic sulfide	Pressed powder pellet, produced by precipitating amorphous metal sulphides from solution with an Fe-Cu-Zn-S matrix	38

($^{34}S/^{32}S$ and $^{33}S/^{32}S$) were calculated by correcting for instrumental mass bias using linear interpolation between the biases calculated from four neighboring standard analyses. All results are expressed in ‰ using delta notation as follows:

$$\delta^{x}S_{V\text{-}CDT}\ [‰] = [(^{x}S/^{32}S)_{sample}/(^{x}S/^{32}S)_{V\text{-}CDT} - 1] \times 1000 \quad (1)$$

where x is 33 and 34, $(^{x}S/^{32}S)_{sample}$ is the measured $^{x}S/^{32}S$ of the sample and $(^{x}S/^{32}S)_{V\text{-}CDT}$ is defined as $(^{34}S/^{32}S)_{V\text{-}CDT} = 0.044163$ and $(^{33}S/^{32}S)_{V\text{-}CDT} = 0.00788$.[40]

3. Results and discussion

3.1 Comparison of signal intensity and precision between the ns- and fs-laser

Fig. 1 illustrates the changes of the ^{32}S signal intensity and $^{34}S/^{32}S$ isotopic ratio as a function of the signal acquisition time obtained under identical MC-ICP-MS conditions for P-S-1 (the pressed powder pellet of IAEA-S-1) and PPP-1 using fs- and ns-LA-MC-ICP-MS. Compared to the average ^{32}S signal intensity of the ns-laser (2.4 J cm^{-2}), fs-laser (1.36 J cm^{-2}) ablation produced higher ^{32}S signal intensities of P-S-1 and PPP-1 by a factor of 2.4 and 1.4, respectively. The ^{32}S signal responses with time between P-S-1 and PPP-1 are also different when using the same laser (Fig. 1a and c). This should be attributed to their different physical and chemical properties. Fig. 1b and d show transient $^{34}S/^{32}S$ ratios of P-S-1 and PPP-1 from 18 to 52 s (time of ablation) in Fig. 1a and c acquired by using the fs- and ns-laser, respectively. The fluctuations of transient $^{34}S/^{32}S$ ratios of PPP-1 and P-S-1 achieved by using the ns-laser were significantly larger than those obtained by using the fs-laser, suggesting that the fs-laser was more suitable for high precision of sulfur isotope analysis in sulfides.

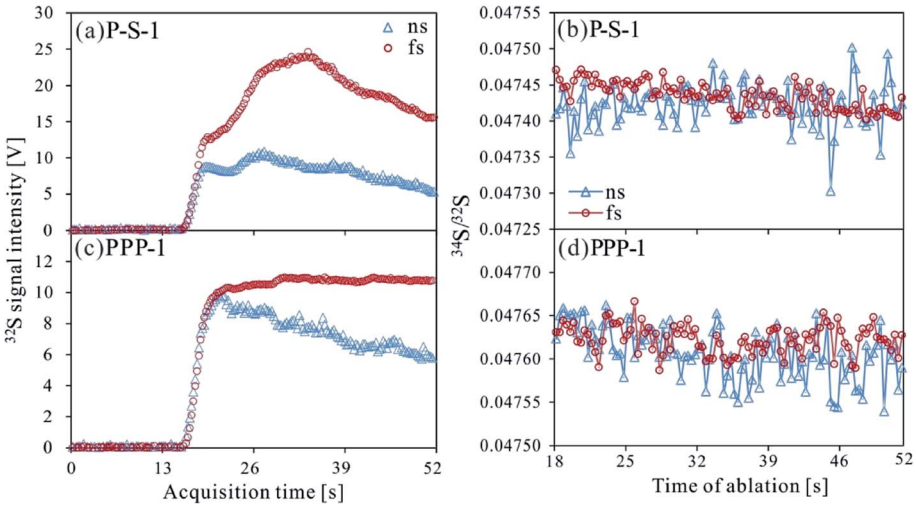

Fig. 1 Transient signal intensity of ^{32}S (a, c) and transient isotopic ratio of $^{34}S/^{32}S$ (b, d) obtained from P-S-1 (44 μm) and PPP-1 (24 μm) at a repetition rate of 3 Hz using the fs-laser (1.36 J cm^{-2}) and ns-laser (2.4 J cm^{-2}) in single spot ablation mode, respectively.

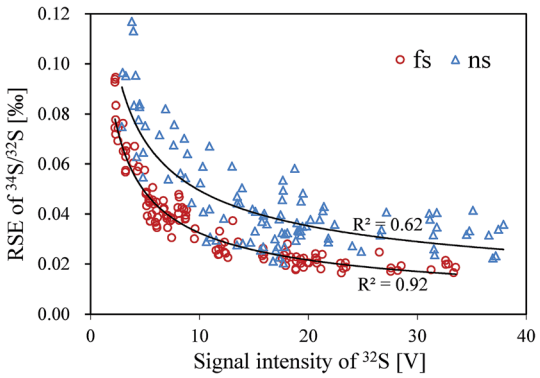

Fig. 2 Comparison of the relationships between the relative standard error (RSE) of $^{34}S/^{32}S$ and the signal intensity of ^{32}S from PPP-1 and P-S-1 measured by using the ns- and fs-laser.

In general, the precision of the measured isotopic ratio is strongly connected to its sensitivity. The ^{32}S signal intensity of the ns- and fs-laser *versus* the corresponding precision ("Relative Standard Error" instead of "precision" here) of $^{34}S/^{32}S$ ratio for *in situ* S isotope analyses is shown in Fig. 2. Clearly, the correlation between the ^{32}S signal intensity and the precision of $^{34}S/^{32}S$ ratio obtained by using the fs-laser fits well into an exponential function with $R^2 = 0.92$, much higher than the correlation coefficient ($R^2 = 0.62$) acquired by using the ns-laser, illustrating the relationship between the ^{32}S sensitivities of the fs-laser and the corresponding precisions conforming to the Poisson distribution. The significant discrete data points acquired by using the ns-laser may be attributed to the incomplete vaporization of large particles produced by the thermal effect of the ns-laser. Compared to the ns-laser, the corresponding average precision of $^{34}S/^{32}S$ ratios achieved by using the fs-laser is improved by a factor of ~1.6 under the same signal intensity conditions. The better internal precision is the result of less fluctuated transient isotopic ratio obtained in single spot analysis by using the fs-laser. For a given analytical precision of 0.04‰ for $^{34}S/^{32}S$, the ^{32}S signal intensity required by using the fs-laser is only 5 V, while that for the ns-laser is 8 V. Therefore, a higher spatial resolution may be achieved by using the fs-laser compared to the ns-laser at the same analytical precision.

3.2 Morphology of ablation craters and aerosol particles by using the ns- and fs-laser

Fig. 3 shows the morphologies of ablation craters and deposited aerosol particles from P-S-1 and PPP-1 generated by using the ns- and fs-laser. These craters were ablated with a 32 μm spot size at a repetition rate of 3 Hz for 200 pulses by using the ns-laser (2.4 J cm^{-2}) and fs-laser (1.36 J cm^{-2}), respectively. As seen in Fig. 3a, there are abundant melted ejecta around the ns-laser crater, and a raised rim around the crater perimeter caused by resolidification of the molten material of P-S-1. The ns-laser has sufficient time for the thermal wave to propagate into the target and can create a recoil pressure by the expended vapor plume

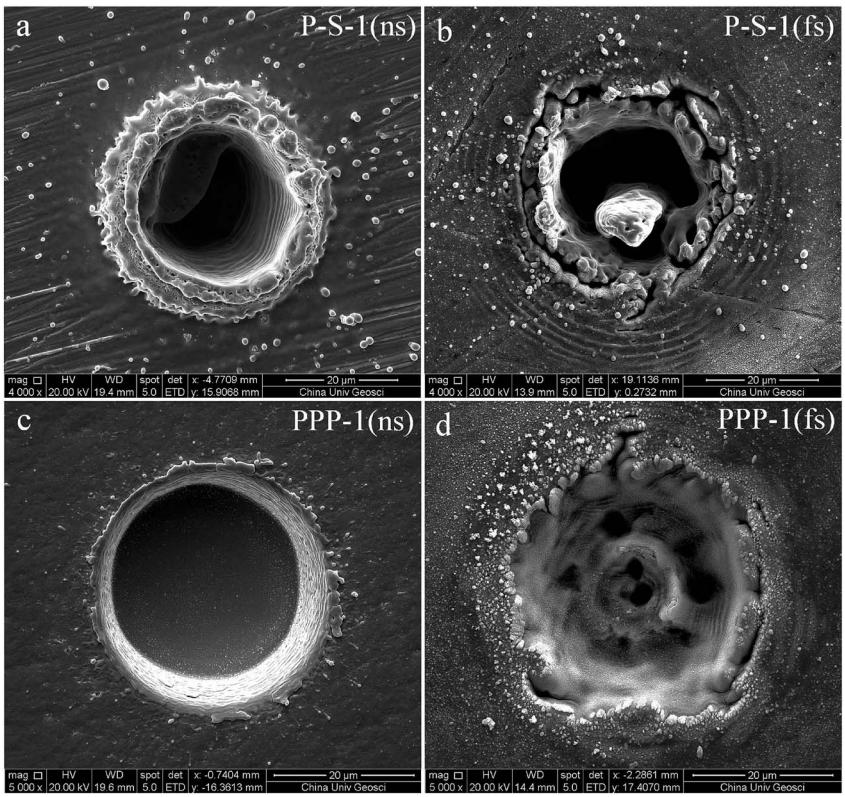

Fig. 3 SEM images of ablation craters in P-S-1 and PPP-1 produced with (a, c) the ns-laser, 32 μm and 2.4 J cm^{-2}; (b, d) the fs-laser, 32 μm and 1.36 J cm^{-2}.

that expels the molten material to form the large droplets and the raised rim around the crater.[41,42] Due to the higher melting point, hardness and stronger bond strengths of PPP-1 than those of P-S-1, the amount of ejecta from PPP-1 ablated by using the ns-laser is significantly less than that of P-S-1, whereas the melting phenomenon can still be readily seen on the crater profiles of PPP-1 (Fig. 3c). In contrast, melting is significantly reduced using the fs-laser regardless of P-S-1 or PPP-1, illustrating the dramatically reduced thermal effects. Moreover, fs-laser crater rims present border deformation, which could be related to the interference between the scattering light and the incident laser light.[25,43] Due to the ns-laser (193 nm excimer laser) beam with a homogeneous energy distribution profile, pan-shaped ablation pits were produced on P-S-1 and PPP-1 (Fig. 3a and c). Unlike in 193 nm excimer laser ablation systems, there is no homogeneous lens in the fs-laser, which has a Gaussian energy beam profile across its diameter. Some small holes and columns within the fs-laser craters are observed (Fig. 3b and d). The self-focusing/defocusing and the highly nonlinear processes of spatial and temporal splitting of fs-laser pulses during propagating inside the samples have been proposed to explain these phenomena.[44]

Fig. 4 shows magnified views of ns- and fs-laser crater rims and ejected particles in Fig. 3a and b. There is a significant difference in the size and structure of the aerosol particles generated by using the ns- and fs-laser. Most of the large spherical aerosol particles (~1–2 μm) deposited around the ns crater rims equip with a small tail (Fig. 4a and b), caused by the rapid movement of unsolidified droplets when they sputtered on the sulfide sample surface. These typical melting phenomena indicate that thermal processes are the dominant mechanisms of sulfide ablation in the ns-laser. In contrast, the fs-laser crater is mainly surrounded by fine aerosol particles (~85 nm) (Fig. 4c). There are also some large aerosol particles (0.5–1 μm) around the fs-laser crater. The magnified view of such large aerosol particles showed that they were formed by agglomeration of fine particles (Fig. 4d). The rough shapes of these fine particles (Fig. 4d) suggest that they may condense quickly and not be affected by heating. These results confirm that the fs-laser is less prone to thermal effects, and produces smaller aerosol particles for the ablation of sulfide samples in comparison with the ns-laser. Thus, the improved sulfur signal sensitivity and $^{34}S/^{32}S$ ratio precision (Fig. 1 and 2) by using the fs-laser should be mainly attributed to the higher aerosol particle transportation efficiency and their improved ionization efficiency in ICP due to the significantly reduced particle sizes.

3.3 Effects of ns- and fs-laser fluence on isotopic fractionation

In general, the characteristics of laser ablation and aerosol particle generation are strongly linked with the fluence deposited at the target sample.[45–47] The fluence has a significant effect on the degree of laser-induced fractionation.[45,46,48] Fig. 5 shows the variation of the measured $^{34}S/^{32}S$ ratios as a function of laser fluence from P-S-1, PPP-1, P-GBW07268, P-GBW07270 and

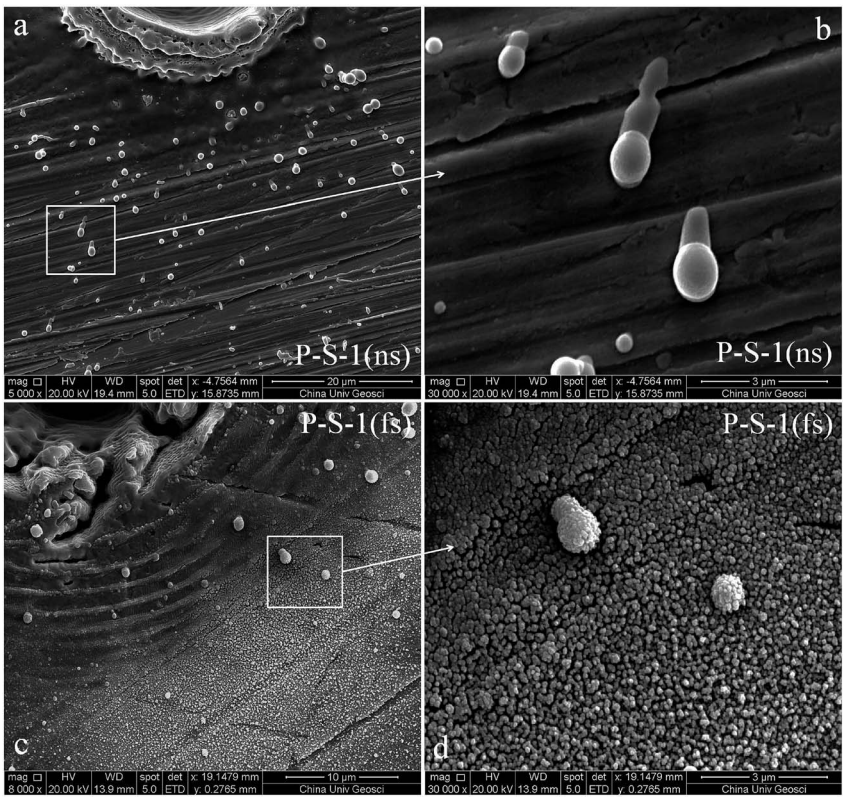

Fig. 4 SEM images of ablation crater rims and ejected particles in P-S-1 produced with (a, b) the ns-laser, 32 μm and 2.4 J cm^{-2}; (c, d) the fs-laser, 32 μm and 1.36 J cm^{-2}; (b) shows the details of (a), and (d) shows the details of (c).

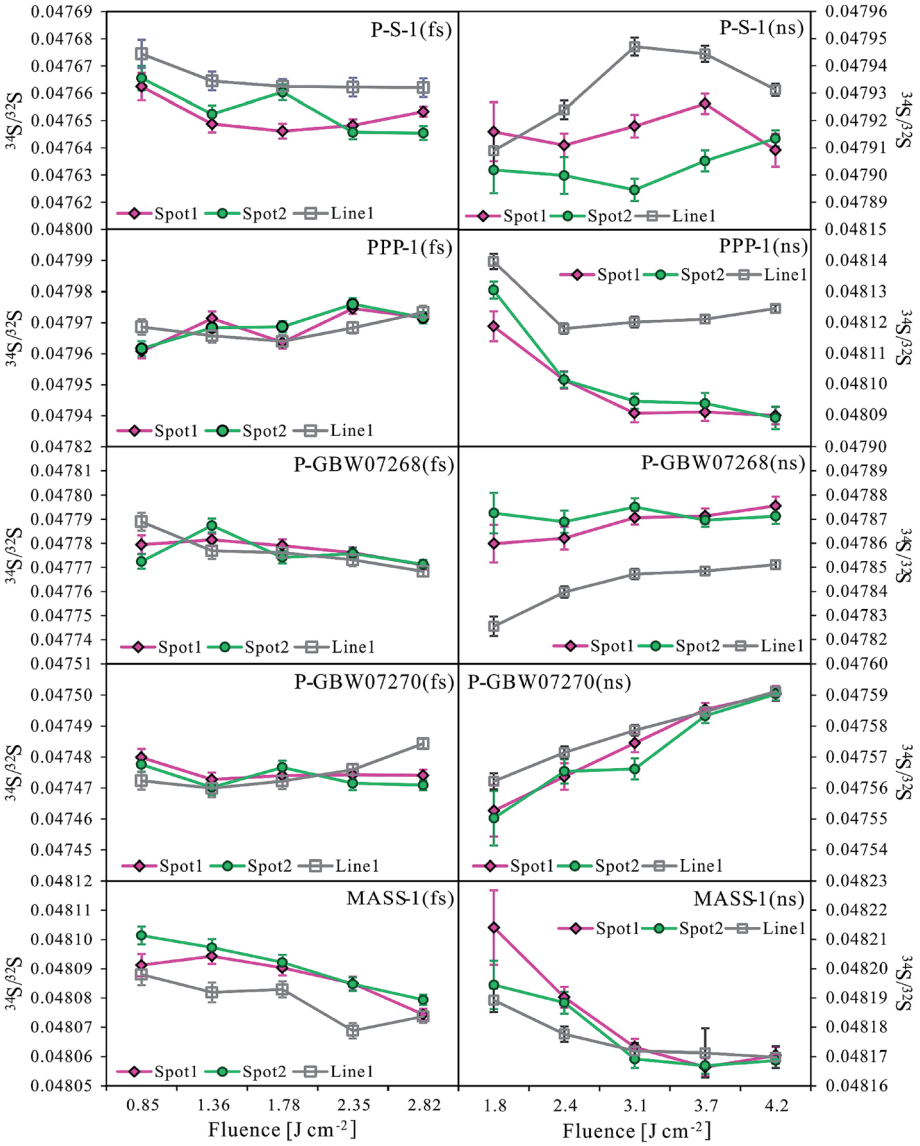

Fig. 5 Comparison of the measured $^{34}S/^{32}S$ ratios from five sulfides as a function of laser fluence at different ablation modes between the ns- and fs-laser. Spot1, Spot2 and Line1 represent continuous two measurements in the single spot ablation mode, followed by a line scanning measurement. Error bars represent within-run precision (2 s).

MASS-1 at both single spot and line scan ablation modes using the ns- and fs-laser, respectively. For the fs-laser, there was almost no fluence dependent isotopic fractionation for these sulfides over a range of fluence from 0.85 to 2.82 J cm^{-2}, except for MASS-1 whose determined $^{34}S/^{32}S$ ratios were slightly decreased with an increase of the laser fluence. However, significant fluence dependent sulfur isotopic fractionations were observed with the ns-laser at fluences of 1.8–4.2 J cm^{-2}. For example, the determined $^{34}S/^{32}S$ ratios of P-GBW07268 and P-GBW07270 are increased with increasing the laser fluences from 1.8 to 4.2 J cm^{-2}, while those of PPP-1 and MASS-1 are significantly decreased with increasing the laser fluences. Moreover, the $^{34}S/^{32}S$ ratios of all the samples measured at all laser fluences with single spot ablation mode were almost identical to those by line scan ablation mode for the fs-laser. In contrast, the determined $^{34}S/^{32}S$ ratios of P-S-1, PPP-1, and P-GBW07268 were significantly different for these two different ablation modes by using the ns-laser at these laser fluences. The analytical precisions were deteriorated for both ns and fs laser systems at low fluences. This is particularly true for the ns-laser due to its lower and less stable signal intensity. The above results confirm that ns-laser sampling is more susceptible to laser-induced fractionation effects relative to the fs-laser for sulfide analysis. The much less dependency on laser fluence and matrix properties of S isotopic fractionation by using the fs-laser may be attributed to the dramatically depressed thermal effects and the produced smaller aerosol particles compared to the ns-laser (Fig. 3 and 4).

3.4 Effect of the makeup gas flow rate on the matrix effect

The incomplete aerosol or particle excitation in the ICP was one of the dominant processes that affected elemental/isotopic

fractionation during laser ablation ICP-MS analysis.[33,49] The nebulizer gas flow rate (makeup gas flow rate) is one of the most important parameters that have a significant effect on ICP properties.[50–52] The measured ^{32}S signal intensity, $\delta^{34}S$ and $\delta^{33}S$ as a function of the makeup gas flow rate from four different matrix sulfides (PPP-1, P-GBW07270, P-GBW07268, and MASS-1) by using the fs-laser are illustrated in Fig. 6. P-S-1 was used as the external calibration standard for these sulfides. The ^{32}S maximum sensitivities of these four sulfides occurred at the same makeup gas flow rate of 0.60 l min^{-1}, suggesting that the locations of zones of maximum ^{32}S ion density formed in the ICP are matrix independent, in agreement with the result that the lightest or most volatile elements did not shift the optimum gas flow rate induced by different matrices reported by Rodushkin *et al.* (2002).[53] The measured $\delta^{34}S$ or $\delta^{33}S$ values exhibited significant deviation from their reference values at high makeup gas flow rates (≧0.60 l min^{-1}), especially for the PPP-1 and P-GBW07270, indicating that the matrix effect is severe at a high makeup gas flow rate, even at the optimum makeup gas flow rate corresponding to the maximum sensitivity of ^{32}S for PPP-1 and P-GBW07270. However, at low makeup gas flow rates (0.52–0.54 l min^{-1}), all the measured $\delta^{34}S$ and $\delta^{33}S$ values of these four sulfides were generally in good agreement with their reference values. The sensitivity of ^{32}S was reduced by up to ~30–40% at the selected low makeup gas flow rates. Compared to the obtained signal enhancement factor of 3.6 by the use of the Jet sample cone in combination with the X skimmer cone,[15] this reduction of the S sensitivity by adopting the low makeup gas flow rates is minimal. Generally, a low makeup gas flow rate means a robust plasma condition.[50,54] This study suggests that the ICP induced S isotopic fractionation among different sulfides can be significantly suppressed when the operating parameters (*e.g.*, makeup gas flow rate) are optimized to generate a sufficient gas temperature in the central channel of the ICP. These results also indicate that the robust plasma condition is a prerequisite for the accurate determination of sulfur isotopes ($\delta^{33}S$ and $\delta^{34}S$) in sulfides by femtosecond laser ablation MC-ICP-MS with non-matrix matched calibration. Note that nitrogen (4–6 ml min^{-1}) was added to the central channel gas of ICP in this study. Fu *et al.* (2016)[15] reported that the addition of 4 ml min^{-1} N_2 to the central gas flow in LA-MC-ICP-MS can efficiently reduce polyatomic interference and stabilize the mass bias for sulfur isotope analysis. It was found that N_2 has a higher thermal conductivity than that of argon by a factor of 32 at 7000 K.[55,56] It is therefore possible that the reduced ICP induced S isotopic fractionation among different sulfides partly results from the increased thermal conductivity which causes a higher plasma temperature, and thus higher ionization efficiency of the aerosol particles.

3.5 Results of reference materials analyzed with non-matrix matched calibration

To verify non-matrix matched calibration capability for S isotope analysis of S-rich samples at high spatial resolution under the robust conditions (at the low makeup gas flow rate of 0.54 l min^{-1}) by fs-LA-MC-ICP-MS, six reference materials of different matrices were analyzed at a fluence of ~1.36 J cm^{-2} with spot sizes of 20–44 μm at the single spot ablation mode. The samples were calibrated against PPP-1, except for PPP-1,

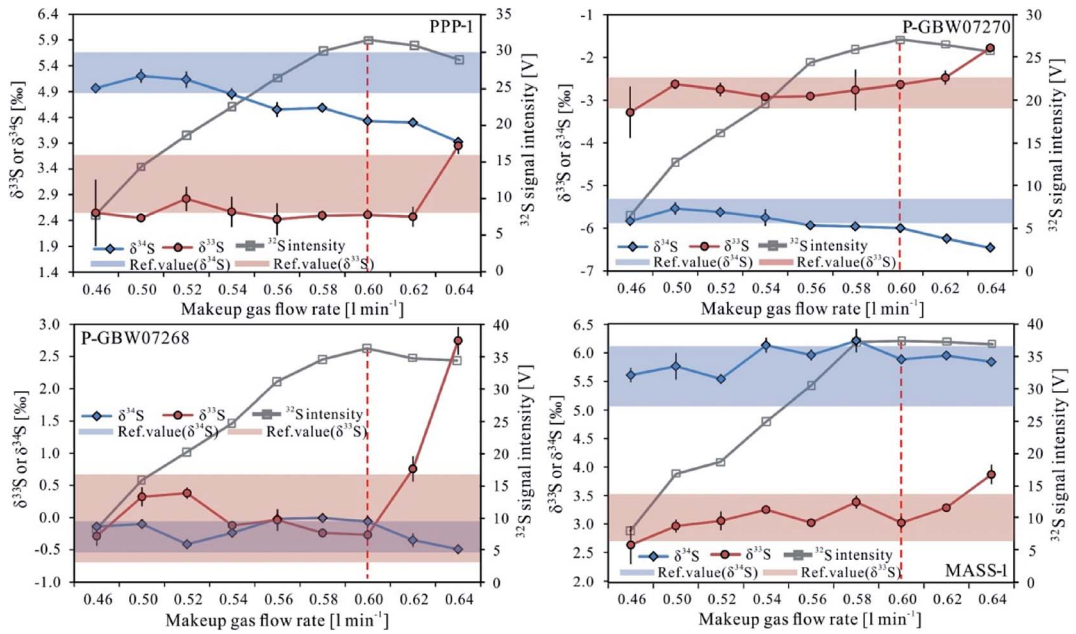

Fig. 6 Effects of the makeup gas flow rate on the measured $\delta^{34}S$, $\delta^{33}S$ and ^{32}S signal intensity from four different matrix sulfides (PPP-1, P-GBW07270, P-GBW07268, and MASS-1) using P-S-1 as the calibration standard by using the fs-laser (44 μm, 1.21 J cm^{-2}, 3 Hz). The red vertical dashed line in each panel shows the optimum makeup gas flow rate, which yield the maximum signal intensity of ^{32}S. The horizontal red and grey shadows in each panel represent the reference values of $\delta^{33}S$ and $\delta^{34}S$ and 2 s error of each sample, respectively. Error bars represent the standard deviation (2 s) of three measurements.

which was calibrated against P-S-1. Fig. 7 shows a compilation of the measured $\delta^{33}S$ and $\delta^{34}S$ (n = 30–35) values that were obtained for these six S-rich reference materials over the course of this study (approximately six months) by fs-LA-MC-ICP-MS. The measured $\delta^{33}S$ and $\delta^{34}S$ of these samples are in excellent agreement with the reference values.[15,22,35,36] The determined $\delta^{33}S$ values in P-S-2 and P-S-4 are exceptions, which significantly deviated from the reference values by using the ns-laser.[15] The determined $\delta^{33}S$ value of P-S-2 by using the fs-laser is consistent with the reference value by using a gas-source mass spectrometer,[35] confirming our value is correct. To further evaluate the accuracy of the determined values by ns- and fs-LA-MC-ICP-MS, the analytical results of these six reference materials are plotted in a $\delta^{33}S$ *versus* $\delta^{34}S$ diagram to show deviations from the trend expected for the mass-dependent fractionation line (MDF) (Fig. 8). This three-isotope plot is often used in stable isotope studies to confirm analytical accuracy.[19] As these reference materials are all young samples, their expected results should fall on the MDF based on the previous studies.[14,57] Clearly, all the results broadly fit to the MDF, except for the

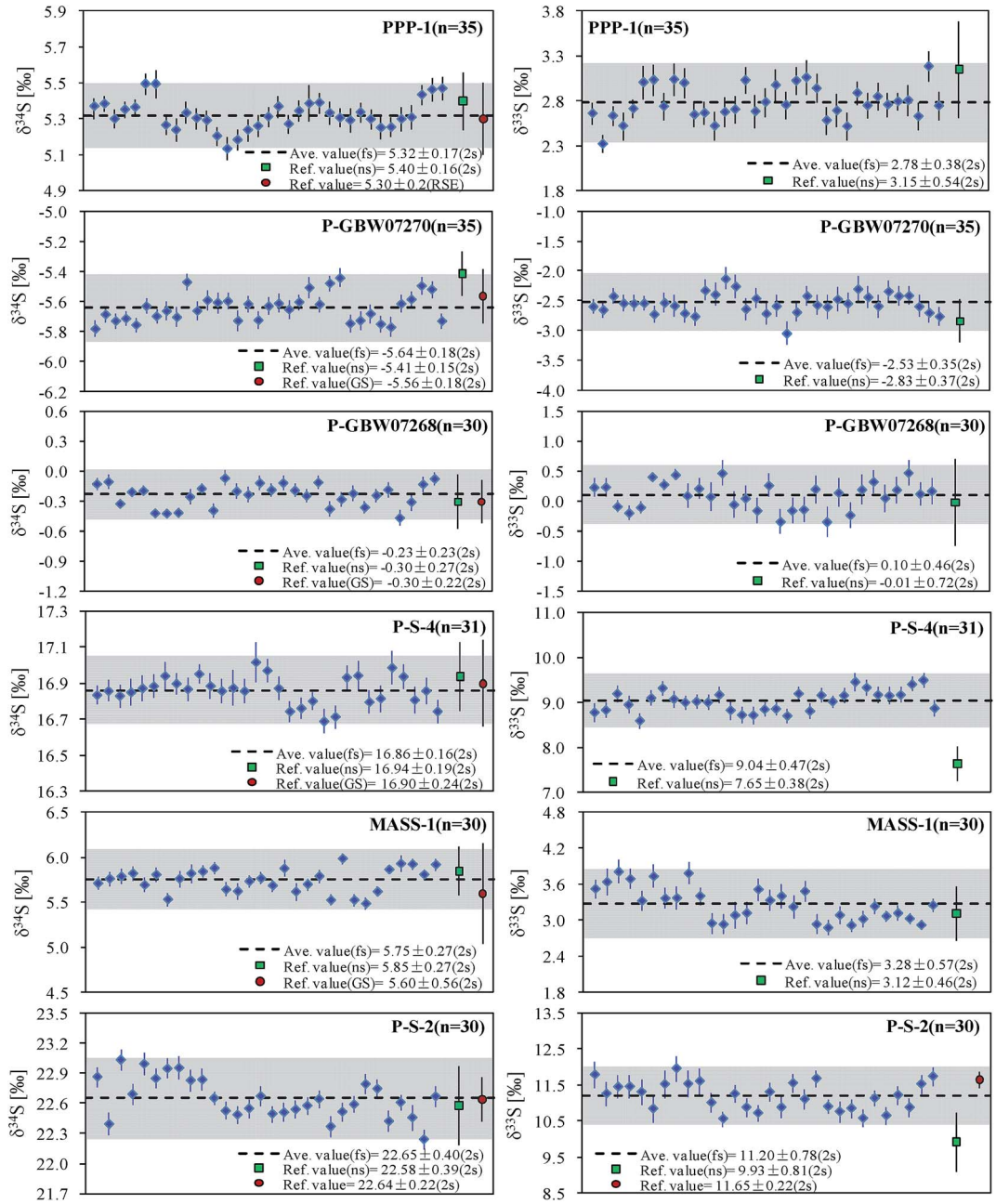

Fig. 7 The measured $\delta^{33}S$ and $\delta^{34}S$ of six reference materials by using the fs-laser. The black horizontal dashed line and grey area in each panel represent the determined average $\delta^{33}S$ or $\delta^{34}S$ value and its 2 s error in the study, respectively. The green square and red circle represent the value measured by using the ns-laser reported in Fu *et al.* (2016)[15] and the recommended values in the literature[22,35,36] for these reference materials, respectively.

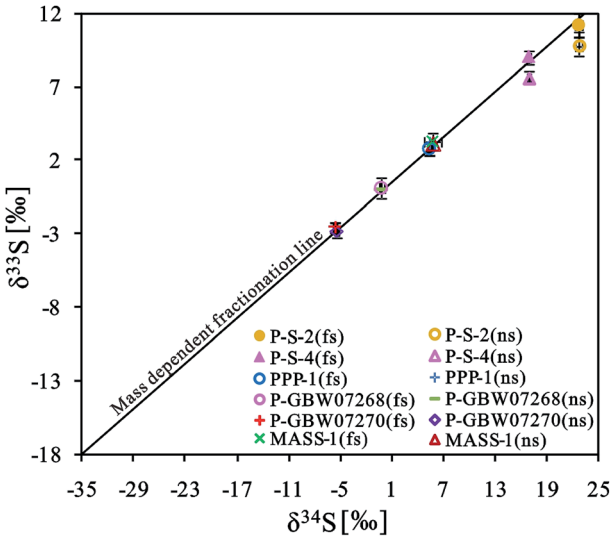

Fig. 8 A plot of the measured $\delta^{33}S$ and $\delta^{34}S$ for six reference materials using the ns-laser in Fu *et al.* (2016)[15] and the fs-laser in this study. The full line is the mass-dependent fractionation line. Error bars represent the standard deviation (2 s).

results of P-S-2 and P-S-4 measured by ns-LA-MC-ICP-MS[15] which show distinctly negative deviation from the MDF, suggesting the biased $\delta^{33}S$ results of P-S-2 and P-S-4 by ns-LA-MC-ICP-MS. These results show that the fs-laser is superior to the ns-laser for sulfur isotope analysis. The excellent long-term accuracies (0.01–0.15‰ for $\delta^{34}S$ and 0.11–0.45‰ for $\delta^{33}S$) and precisions (0.16–0.40‰ for $\delta^{34}S$ and 0.35–0.78‰ for $\delta^{33}S$, 2 s) of the determined values in these different S-rich reference materials demonstrated that the proposed analytical protocol with non-matrix matched calibration for sulfur isotope analysis by fs-LA-MC-ICP-MS at high spatial resolutions of 20–44 μm is feasible.

4. Conclusions

The results presented here indicate that non-matrix matched calibration for accurate sulfur isotope analysis in S-rich samples is feasible by fs-LA-MC-ICP-MS in combination with the robust plasma conditions. Compared to ns-LA-MC-ICP-MS, higher sensitivity (1.4–2.4 times) under similar instrumental conditions and better precision (~1.6-fold) under the same signal intensity conditions were achieved by fs-LA-MC-ICP-MS. Moreover, the less thermal effect and the smaller particles in the fs-laser were observed from the morphologies of ablation craters and ejected particles produced by using the fs- and ns-laser under similar instrumental conditions. No significant fluence and matrix dependent sulfur isotopic fractionation for these sulfides with different matrices were observed with the fs-laser. Thus, better results obtained by fs-LA-MC-ICP-MS are attributed to the less thermal effect and the smaller particles generated in the fs-laser which resulted in more efficient transportation and ionization. The matrix effect was still observed in fs-LA-MC-ICP-MS under themaximum sensitivity conditions. However, application of the robust plasma conditions (*e.g.*, at a lower makeup gas flow rate) can significantly reduce the matrix effect for S isotope analysis. The results obtained from six reference materials with different matrices by fs-LA-MC-ICP-MS using non-matrix matched calibration show excellent agreement with the reference values and the mass-dependent fractionation line with spot sizes of 20–44 μm, demonstrating the capability of this developed method for achieving reliable *in situ* S isotope measurements in S-rich samples at high spatial resolution.

Conflicts of interest

There are no conflicts of interest to declare.

Acknowledgements

We would like to thank Sarah Gilbert for providing the pyrite PPP-1 reference material. This research is supported by the National Key R&P Plan (2016YFE0203000), the National Science Fund for Distinguished Young Scholars and the National Natural Science Foundation of China (Grants 41573015 and 41322023), the Science Fund for Distinguished Young Scholars of Hubei Province (2016CFA047), and the MOST Special Fund from the State Key Laboratories of Geological Processes and Mineral Resources.

References

1 R. E. Russo, X. Mao, H. Liu, J. Gonzalez and S. S. Mao, *Talanta*, 2002, **57**, 425–451.
2 D. Günther, I. Horn and B. Hattendorf, *Fresenius' J. Anal. Chem.*, 2000, **368**, 4.
3 I. Horn, F. von Blanckenburg, R. Schoenberg, G. Steinhoefel and G. Markl, *Geochim. Cosmochim. Acta*, 2006, **70**, 3677–3688.
4 Z. C. Hu, Y. S. Liu, S. Gao, W. G. Liu, W. Zhang, X. R. Tong, L. Lin, K. Q. Zong, M. Li, H. H. Chen, L. Zhou and L. Yang, *J. Anal. At. Spectrom.*, 2012, **27**, 1391–1399.
5 C. W. Mandeville and C. W. Mandeville, *Elements*, 2010, **6**, 75–80.
6 B. Mayer and H. R. Krouse, *Handb. Stable Isot. Anal. Tech.*, 2004, 538–596.
7 M. Berglund and M. E. Wieser, *Pure Appl. Chem.*, 2011, **83**, 397–410.
8 R. R. Seal, *Rev. Mineral. Geochem.*, 2006, **61**, 633–677.
9 S. Ono, B. Wing, D. Johnston, J. Farquhar and D. Rumble, *Geochim. Cosmochim. Acta*, 2006, **70**, 2238–2252.
10 D. Tanner, R. W. Henley, J. A. Mavrogenes and P. Holden, *Contrib. Mineral. Petrol.*, 2016, **171**, 33.
11 R. Clough, P. Evans, T. Catterick and E. H. Evans, *Anal. Chem.*, 2006, **78**, 6126–6132.
12 M. Yun, M. A. Wadleigh and A. Pye, *Chem. Geol.*, 2004, **204**, 369–376.
13 M. Peters, H. Strauss, J. Farquhar, C. Ockert, B. Eickmann and C. L. Jost, *Chem. Geol.*, 2010, **269**, 180–196.
14 B. Bühn, R. V. Santos, M. A. Dardenne and C. G. de Oliveira, *Chem. Geol.*, 2012, **312–313**, 163–176.

15 J. L. Fu, Z. C. Hu, W. Zhang, L. Yang, Y. S. Liu, M. Li, K. Q. Zong, S. Gao and S. H. Hu, *Anal. Chim. Acta*, 2016, **911**, 14–26.
16 T. Ushikubo, K. H. Williford, J. Farquhar, D. T. Johnston, M. J. Van Kranendonk and J. W. Valley, *Chem. Geol.*, 2014, **383**, 86–99.
17 J. M. Eiler, C. Graham and J. W. Valley, *Chem. Geol.*, 1997, **138**, 221–244.
18 M. Shaheen and B. J. Fryer, *J. Anal. At. Spectrom.*, 2010, **25**, 1006.
19 P. R. D. Mason, J. Košler, J. C. M. de Hoog, P. J. Sylvester and S. Meffan-Main, *J. Anal. At. Spectrom.*, 2006, **21**, 177–186.
20 P. R. Craddock, O. J. Rouxel, L. A. Ball and W. Bach, *Chem. Geol.*, 2008, **253**, 102–113.
21 C. Bendall, Y. Lahaye, J. Fiebig, S. Weyer and G. P. Brey, *Appl. Geochem.*, 2006, **21**, 782–787.
22 S. E. Gilbert, L. V. Danyushevsky, T. Rodemann, N. Shimizu, A. Gurenko, S. Meffre, H. Thomas, R. R. Large and D. Death, *J. Anal. At. Spectrom.*, 2014, **29**, 1042–1051.
23 Z. Y. Zhu, S. Y. Jiang, C. L. Ciobanu, T. Yang and N. J. Cook, *Chem. Geol.*, 2017, **450**, 223–234.
24 I. Horn and F. von Blanckenburg, *Spectrochim. Acta, Part B*, 2007, **62**, 410–422.
25 Z. Li, Z. C. Hu, D. Günther, K. Q. Zong, Y. S. Liu, T. Luo, W. Zhang, S. Gao and S. H. Hu, *Geostand. Geoanal. Res.*, 2016, **40**, 477–491.
26 V. Možná, J. Pisonero, M. Holá, V. Kanický and D. Günther, *J. Anal. At. Spectrom.*, 2006, **21**, 1194–1201.
27 B. Fernández, F. Claverie, C. Pécheyran, O. F. X. Donard and F. Claverie, *TrAC, Trends Anal. Chem.*, 2007, **26**, 951–966.
28 M. E. Shaheen, J. E. Gagnon and B. J. Fryer, *Chem. Geol.*, 2012, **330–331**, 260–273.
29 J. Chmeleff, I. Horn, G. Steinhoefel and F. von Blanckenburg, *Chem. Geol.*, 2008, **249**, 155–166.
30 L. Chen, K. Chen, Z. Bao, P. Liang, T. Sun and H. L. Yuan, *J. Anal. At. Spectrom.*, 2017, **32**, 107–116.
31 S. E. Jackson and D. Günther, *J. Anal. At. Spectrom.*, 2003, **18**, 205–212.
32 H.-R. Kuhn, N. J. Pearson and S. E. Jackson, *J. Anal. At. Spectrom.*, 2007, **22**, 547.
33 J.-I. Kimura, Q. Chang, T. Ishikawa and T. Tsujimori, *J. Anal. At. Spectrom.*, 2016, **31**, 2305–2320.
34 Z. C. Hu, W. Zhang, Y. S. Liu, S. Gao, M. Li, K. Q. Zong, H. H. Chen and S. H. Hu, *Anal. Chem.*, 2015, **87**, 1152–1157.
35 T. P. Ding, S. Valkiers, D. F. Wan, R. M. Bai, X. Q. Zou, Y. H. Li, Q. L. Zhang and P. De Bièvre, *Bull. Mineral., Petrol. Geochem.*, 2001, **20**, 425–427.
36 H. P. Qi and T. B. Coplen, *Chem. Geol.*, 2003, **199**, 183–187.
37 Research Group of Sulphide Mineral Reference Materials, *Rock Miner. Anal.*, 1995, **14**, 81–113.
38 S. A. Wilson, W. I. Ridley and A. E. Koenig, *J. Anal. At. Spectrom.*, 2002, **17**, 406–409.
39 S. Weyer and J. B. Schwieters, *Int. J. Mass spectrom.*, 2003, **226**, 355–368.
40 T. P. Ding, S. Valkiers, H. Kipphardt, P. De Bièvre, P. D. P. Taylor and R. Gonfiantini, *Geochim. Cosmochim. Acta*, 2001, **65**, 2433–2437.
41 C. Liu, X. L. Mao, S. S. Mao, X. Zeng, R. Greif and R. E. Russo, *Anal. Chem.*, 2004, **76**, 379–383.
42 B. N. Chichkov, C. Momma, S. Nolte, F. Von Alvensleben and A. Tünnermann, *Appl. Phys. A: Mater. Sci. Process.*, 1996, **63**, 109–115.
43 F. Poitrasson, X. Mao, S. S. Mao, R. Freydier and R. E. Russo, *Anal. Chem.*, 2003, **75**, 6184–6190.
44 S. S. Mao, F. Quéré, S. Guizard, X. Mao, R. E. Russo, G. Petite and P. Martin, *Appl. Phys. A: Mater. Sci. Process.*, 2004, **79**, 1695–1709.
45 P. K. Diwakar, J. J. Gonzalez, S. S. Harilal, R. E. Russo and A. Hassanein, *J. Anal. At. Spectrom.*, 2014, **29**, 339–346.
46 Q. Bian, C. C. Garcia, J. Koch and K. Niemax, *J. Anal. At. Spectrom.*, 2006, **21**, 187–191.
47 N. L. Lahaye, M. C. Phillips, A. M. Duffin, G. C. Eiden and S. S. Harilal, *J. Anal. At. Spectrom.*, 2015, **31**, 515–522.
48 Z. Li, Z. Hu, Y. Liu, S. Gao, M. Li, K. Zong, H. Chen and S. Hu, *Chem. Geol.*, 2015, **400**, 11–23.
49 M. Guillong and D. Günther, *J. Anal. At. Spectrom.*, 2002, **17**, 831–837.
50 I. I. Stewart and J. W. Olesik, *J. Anal. At. Spectrom.*, 1998, **13**, 1313–1320.
51 S. H. Tan and G. Horlick, *J. Anal. At. Spectrom.*, 1987, **2**, 745–763.
52 H. Andrén, I. Rodushkin, A. Stenberg, D. Malinovsky and D. C. Baxter, *J. Anal. At. Spectrom.*, 2004, **19**, 1217–1224.
53 I. Rodushkin, M. D. Axelsson, D. Malinovsky and D. C. Baxter, *J. Anal. At. Spectrom.*, 2002, **17**, 1223–1230.
54 C. Agatemor and D. Beauchemin, *Spectrochim. Acta, Part B*, 2011, **66**, 1–11.
55 S. F. Durrant, *Fresenius' J. Anal. Chem.*, 1994, **349**, 768–771.
56 S. Greenfield, I. L. Jones, H. McGreachin and P. B. Smith, *Anal. Chim. Acta*, 1975, **74**, 225–245.
57 H. Ohmoto, Y. Watanabe, H. Ikemi, S. R. Poulson and B. E. Taylor, *Nature*, 2006, **442**, 908–911.